Electronic Structural Insight into High-Performance Quantum Dot Light-Emitting Diodes

Yang Cheng, Zhixiang Gui, Ruixi Qiao, Shucheng Fang, Guohang Ba, Tianyu Liang, Haoyue Wan, Zhihong Zhang, Can Liu, Chaojie Ma, Hao Hong,* Fengjia Fan,* Kaihui Liu,* and Huaibin Shen*

Quantum dot light-emitting diodes (QD-LEDs) are highly promising light sources with excellent figures of merit. Although great successes have been achieved in elevating some key parameters to an ideal level, QD-LEDs with superior performance in all aspects have rarely been realized. Herein, by exploring crystalline structure-dependent electronic properties, it is shown that QD-LEDs can simultaneously exhibit high external quantum efficiency, roll-off-free under high brightness, and dramatically improved operational stability. This improved performance stems from the crystal phase engineering of QD. Reduced structure symmetry in the wurtzite phase introduces an unneglectable internal crystal field compared with the zinc-blende one, which raises both the conduction and valence band energy levels, thus, facilitating a more balanced charge injection. The crystal phase-optimized superior-comprehensive performance in the QD-LED offers a novel degree of freedom for device engineering and promotes commercial applications for the upcoming display and illumination technologies.

1. Introduction

The characteristics of the size-tunable color, narrow emission spectrum, and high quantum yield (QY) enable colloidal QDs as the upcoming candidates for the light-emitting layer in LEDs.[1–17] Since the first demonstration in 1994, numerous advances have been made in fabricating high-efficiency and high-brightness QD-LEDs with long operational lifetimes. The peak EQE of QD-LEDs has been elevated to the theoretical limit,[18] the brightness has been increased to over 100 000 cd cm^{-2}, which is high enough for lighting applications,[10,19] and the T_{95} operation lifetime (defined as the time for the luminance intensity decreases to 95% of the initial value) has been raised to more than 1000 h.[16,17] However, those parameters can only be partially achieved with a specific design. QD-LEDs with comprehensive high performances are prerequisites for real applications but have yet to be realized.

Crystal phase engineering could potentially serve as a powerful tool to modulate the physical and chemical properties of materials.[20,21] In II–VI and III–V compound bulk materials (e.g., CdSe, CdS, and InP), wurtzite and zinc-blende are two typical crystalline structures, where atomic layers are repeated with ABA stacking in the wurtzite structure while ABC stacking in the zinc-blende counterpart (**Figure 1**a,b). This

Y. Cheng, Z. Gui, G. Ba, H. Shen
Key Laboratory for Special Functional Materials
School of Materials Science and Engineering
Henan University
Kaifeng, China
E-mail: 10330007@vip.henu.edu.cn

Y. Cheng, R. Qiao, T. Liang, H. Wan, C. Liu, C. Ma, H. Hong, K. Liu
State Key Laboratory for Mesoscopic Physics
School of Physics
Peking University
Beijing, China
E-mail: haohong@pku.edu.cn; khliu@pku.edu.cn

S. Fang, F. Fan
CAS Key Laboratory of Microscale Magnetic Resonance and School
of Physical Sciences
University of Science and Technology of China
Hefei, China
E-mail: ffj@ustc.edu.cn

S. Fang
CAS Center for Excellence in Quantum Information and
Quantum Physics
University of Science and Technology of China
Hefei, China

Z. Zhang
Institute for Multidisciplinary Innovation
University of Science and Technology Beijing
Beijing, China

K. Liu
International Center for Quantum Materials
Collaborative Innovation Center of Quantum Matter
Peking University
Beijing, China

K. Liu
Songshan Lake Materials Laboratory
Guangdong, China

The ORCID identification number(s) for the author(s) of this article can be found under https://doi.org/10.1002/adfm.202207974.

**ADVANCED
SCIENCE NEWS**
www.advancedsciencenews.com

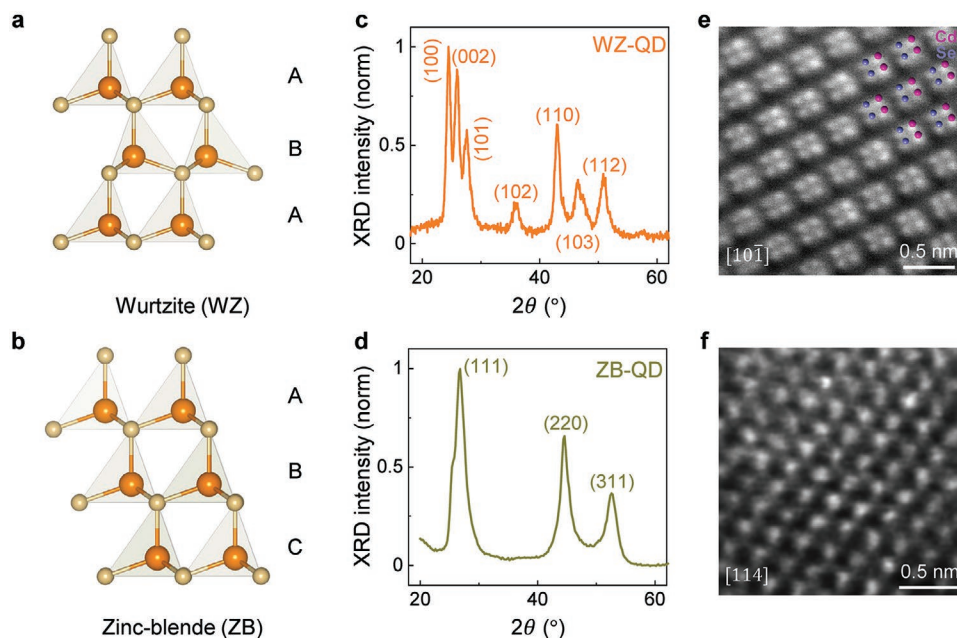**ADVANCED
FUNCTIONAL
MATERIALS**
www.afm-journal.de

Figure 1. Crystal structure characterizations of WZ- and ZB-QD. Scheme of the a) WZ and b) ZB crystal structures. In the wurtzite structure, atom layers are repeated with ABA stacking, while it is ABC stacking for the zinc-blende structure. The normalized XRD 2θ scan spectra of c) WZ- and d) ZB-QD. The presence of (102) and (103) facets in the WZ-QD reveals the wurtzite structure., HAADF-STEM images of e) WZ-QD and f) ZB-QD, matching well with WZ-CdSe along the [10$\bar{1}$] zone axis and ZB-CdSe along the [114] zone axis, respectively. Scale bar, 0.5 nm.

discrepancy leads to reduced structure symmetry and a non-negligible internal crystal field in the wurtzite structure, which has been predicted to be beneficial for the transfer and separation of photogenerated electrons and holes in bulk ZnS.[22] As the electric transport -properties play an essential role in the carrier injection, the elaboration of the crystal structure is believed to be an effective strategy for tuning LED performance based on II–VI and III–V compound QDs. However, the crystal phase-dependent electronic properties of QD and especially the performance of corresponding LED have been rarely explored.

2. Results and Discussion

In our experiments, the wurtzite- (WZ-) and zinc-blende- (ZB-) QD with similar sizes, QYs in solution (>90%), and emission wavelengths (Figures S1–S3. Supporting Information) were synthesized by carefully controlling the nucleation precursor and reaction temperature (see Experimental Section for more details).[23,24] The crystal structures of QDs were determined by the X-ray diffraction (XRD) 2θ scan (Figure 1c,d), where the characteristic peak (102) and (103) facets are present in the WZ-QD but absent in the ZB-QD. This crystal structure difference can be further confirmed with the high-angle annular dark-field scanning transmission electron microscopy (HAADF-STEM) image: the as-grown WZ- and ZB-QD match well with WZ-CdSe along the [10$\bar{1}$] zone axis and ZB-CdSe along the [114] zone axis, respectively (Figure 1e,f). In addition, we performed energy dispersive X-ray spectroscopy (EDS) mapping to characterize the element distributions of QDs. Both the synthesized WZ- and ZB-QD exhibit a near-spherical morphology with a

large size of ≈17 nm (Figures S2 and S3, Supporting Information). The corresponding EDS mappings of Cd, Zn, Se, and S also show similar gradient distributions: Cd and Se atoms are mainly located at the center, while Zn and S atoms are distributed around the outer layer.

With these different crystal structures QDs, both types of QD-LEDs were evaluated by fabricating the prevailing solution-processed organic-inorganic hybrid architecture (**Figure 2**a,b). The current density- and luminance-dependent EQEs of both WZ- and ZB-QD-LEDs are shown in Figure 2c,d. At low current density or luminance, the EQE of both WZ- and ZB-QD-LEDs is close to the theoretical maximum value of 21.9% and 21.6%, respectively. Both devices exhibit efficiency roll-off under further increased current density or luminance. However, the WZ-QD-LEDs show much higher efficiency roll-off current density and luminance threshold than the ZB-QD-LEDs. To quantitatively compare the efficiency roll-off behaviors of the QD-LED, we use J_{95} and L_{95} (current or luminance when EQE drops to the 95% peak value) as two indexes. In contrast to $J_{95} = 49$ mA cm^{-2} and $L_{95} = 18\,000$ cd m^{-2} for the ZB-QD-LED, J_{95} and L_{95} of the WZ-QD-LED are over one order of magnitude higher, reaching ≈600 mA cm^{-2} and 210 000 cd m^{-2}, respectively. To the best of our knowledge, the J_{95} and L_{95} in our WZ-QD-LED are the highest values so far in either the solution-processed QD-LED or OLED (Table S1, Supporting Information). Figure 2e,f presents the voltage-dependent current density (J) and luminance (L) of both types QD-LEDs. The ZB-QD-LED exhibits a turn-on voltage V_T (defined as the required operation voltage with luminance of 1 cd m^{-2}) of 1.9 V and a required voltage of 2.9 V to achieve luminance $L = 1000$ cd m^{-2}. However, the WZ-QD-LED requires a lower turn-on voltage $V_T = 1.7$ V and a much lower voltage of 2.0 V to achieve 1000 cd m^{-2}.
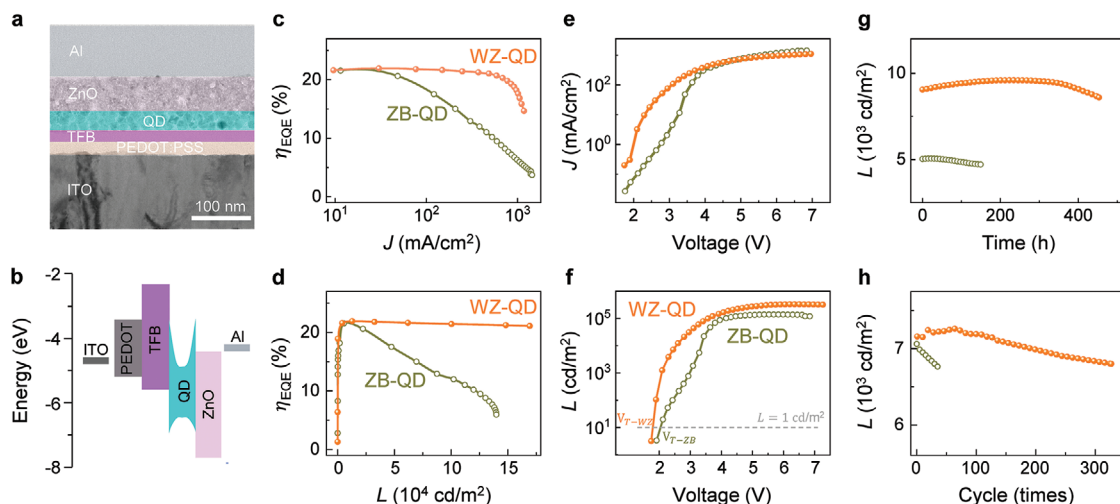
Figure 2. Performance of the WZ- and ZB-QD-LEDs. a) Cross-sectional TEM image and b) energy-band diagram of the QD-LED. Scale bar, 100 nm. c) Current density- and d) luminance- dependent EQE of the QD-LED. The ZB-QD-LED has a better ability to minimize efficiency roll-off compared with the ZB-QD-LED. The voltage V_T of WZ- and ZB-QD, defined as the required operation voltage with the luminance of 1 cd m^{-2}, is added in (d) to ease their identification for the reader. e), Voltage-dependent current density and f) luminance in the QD-LED. For definitive luminance, the ZB-QD-LED (dark yellow) exhibits a lower operation voltage than the WZ-QD-LED (orange). g) The luminance evolution over operation time for the WZ- and ZB-QD-LEDs. The T95 lifetime is prolonged from ≈125 h for the ZB-QD-LED at an initial brightness of L_0 = 5050 cd m^{-2} to ≈450 h for the WZ-QD-LED at L_0 = 9050 cd m^{-2}. h) Luminance of the ZB- and WZ-QD-LEDs recorded over hundreds of switching cycles. The WZ-QD-LED can persist for more than 300 cycles before reducing to 95% with an initial brightness of L_0 = 7150 cd m^{-2}. The operation stability is obviously improved in the WZ-QD-LED compared with the ZB-QD-LED.

Since higher brightness can be achieved at low voltage in the WZ-QD-LED, the LED operating stability can also be improved. With an initial brightness of L_0 = 5050 cd m^{-2}, the ZB-QD-LED exhibits a T_{95} operational lifetime (defined as the time for the luminance decreases to 95% of L_0) of ≈125 h only (Figure 2g). While for the WZ-QD-LED, T_{95} is prolonged to ≈450 h with a higher luminance of L_0 = 9050 cd m^{-2}. Fitting by an empirical equation, $(L_0)^n \times T_{95}$ = constant,[25] acceleration factors n of ≈1.86 and 1.75 are determined for the ZB- and WZ-QD-based devices, respectively (Figure S4, Supporting Information). The extrapolated T_{95} operational lifetime of the WZ-QD-LED at an initial brightness of 1000 cd m^{-2} is estimated to be ≈21 000 h, which is approximately one order of magnitude higher than that of the ZB-QD-LED (≈2500 h) and higher than any other reported values (Table S2, Supporting Information).

Operation cycle stability is another critical parameter to evaluate the operation stability of the QD-LED, as the device usually degrades seriously over a few switching cycles.[8,9] To test the operation cyclability, we fixed the current density at 16 mA cm^{-2} for both WZ- and ZB-QD-LEDs, and turned off, and then on the QD-LEDs every 2 hours, and recorded the luminance over cycle times. For the ZB-QD-LED, the initial brightness (L_0 = 7050 cd m^{-2}) is reduced to 95% after 35 cycles. In contrast, the WZ-QD-LED can persist for more than 300 cycles before reducing to 95% with L_0 = 7150 cd m^{-2} (Figure 2h).

To understand the extraordinarily superior comprehensive performance of our WZ-QD-LEDs, we first investigated the single exciton and biexciton recombination dynamics, since Auger recombination was previously regarded as the dominant factor for the efficiency roll-off at high current density.[19] The WZ- and ZB-QDs with similar absorption cross-sections (Figure S5, Supporting Information) were spin-coated on a glass

substrate for comparison. From the pump fluence-dependent PL decay measurements (**Figure 3**b), we observe similar multiple exciton dynamics in WZ- and ZB-QDs, which can be fitted with a biexponential function $y = y_0 + A_1 e^{-(x-x_0)/t_1} + A_2 e^{-(x-x_0)/t_2}$. The slow decay component t_2 and fast decay component t_1 are attributed to the single and biexciton decay,[26–28] respectively, and they are similar in the two types of QDs (Table S3, Supporting Information). In addition, the ratios of A_1/A_2 at the same pump fluence of both QDs are almost identical and increase with higher pump fluence. The similar multiple exciton dynamics in both WZ- and ZB-QDs suggest that the loss through Auger recombination should also be identical, and thus, the difference in device performance is not attributed to Auger recombination dynamics under photoexcitation only.

In the working LEDs, however, the optical and electrical properties of QDs are remarkably different from our simultaneous in-situ photoluminescence (PL) and electroluminescence (EL) measurements. The QD-LED was under continuous electrical injection, and simultaneously the photoexcitation was kept low to avoid introducing additional charges and used as a non-invasive probe to detect the charging state of the QD (Figure 3a). After carefully analyzing the dependence of the normalized EQE and PL intensity at different bias voltages, a strong correlation between them is observed in the two types of QD-LEDs, indicating that the QD-LED roll-off behavior stems from the PL efficiency attenuation of the QD layer (Figure 3c).

Two prevailing scenarios have been proposed to understand the PL efficiency roll-off in the working QD-LED under high voltages: the quantum-confined Stark effect (QCSE) and charge injection imbalance.[29,30] QCSE describes the effect that the external electric field will decrease the electron-hole overlap integral and reduce their recombination efficiency. To
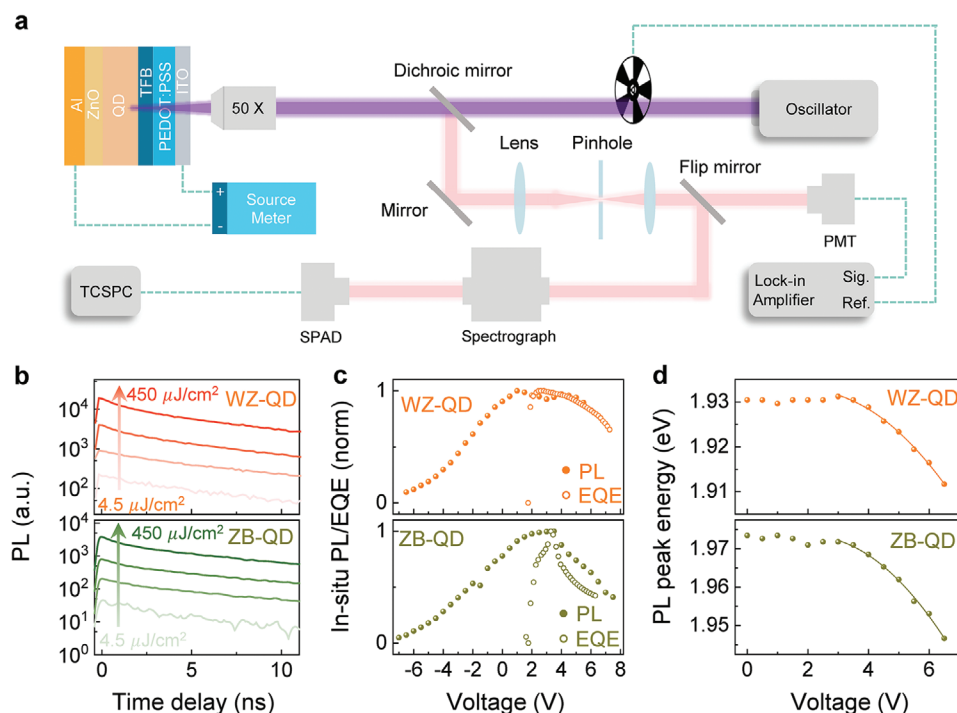
Figure 3. Simultaneous in situ PL and EL spectroscopy. a) Scheme of simultaneously in situ PL and EL experiments. Electrical excitation and optical excitation are simultaneously applied to the QD-LED. To isolate the pure in situ PL signal in the working device, we utilize spatial filtering (4f confocal system and pinhole) and lock-in technologies together. b) Pump fluence-dependent transient PL measurements of WZ- and ZB-QDs. As we increase the pump fluence from 4.5 μJ cm^{-2} to 450 μJ cm^{-2}, the WZ- and ZB-QDs exhibit a transition from slow to fast decay under a similar pump fluence. c) Normalized EQE and in situ PL intensity as functions of applied voltage in the working QD-LED. The in situ PL intensity has nearly the same tendency as the EQE curve, indicating that the charging status has a great influence on the EQE of the two types of QDs. d) The voltage-dependent PL peak energy of WZ- (orange sphere) and ZB-QD-LED (dark yellow sphere). Both types of QD-LEDs show similar PL peak energy redshifts. The quadratic fitting curves of WZ- and ZB-QD are added when the voltage is above 3 V.

investigate whether the different roll-off behaviors are related to QCSE, we further monitored the PL spectra of two types of QD-LEDs at positive voltages (Figure 3d). Both PL peaks of WZ- and ZB-QDs show a quadratic dependence on voltage (orange and yellow line fits, respectively), which is an obvious signature of the QCSE.[31] We observe a similar dependence of the PL energy shifts and peak intensities on the voltage between the two types of QD-LEDs, thus concluding that the QCSE is also not the prominent cause for the difference in PL and EL efficiency.

To confirm whether the charge injection imbalance is the dominant factor affecting EL efficiency, we then investigated the intrinsic electronic properties of the two types of QDs through ultraviolet photoelectron spectroscopy (UPS) and single-carrier device measurements. The UPS is a widely-used technique to analyze the HOMO energy level in QDs,[17,32] and we took multiple tests and averaged the results for both WZ- and ZB-QD to minimize the measurement error (Figure S6, Supporting Information). The highest occupied molecular orbital (HOMO) energy level of the ZB-QD is ≈0.2 eV higher than that of the WZ-QD in UPS spectra (**Figure 4**a). As these two QDs have similar emission wavelengths and hence bandgaps, the lowest unoccupied molecular orbital (LUMO) energy level should also be ≈0.2 eV higher in the ZB-QD. This result agrees well with our observation from single-carrier device measurements: hole

transport is promoted in the WZ-QD-based devices, while electron transport is depressed (Figure 4b,c).

The charge injection balance will potentially influence the charging state of QD and EQE in the QD-LED and hence optimize the roll-off behaviors in the QD-LED, considering that electron injection is usually overwhelmingly more efficient than the hole.[8,33] Although both types of QDs with similar absorption cross-sections have the same Auger recombination rate when photoexcited at the same pump fluence (Figure 3b), the charge population will be different in the working LED when the electron and hole injections are imbalanced, and loss through Auger recombination and electron leakage may vary significantly. At a low voltage range (from 0 to 1 V), as shown in Figure 3c, the PL intensity increases in the two types of QDs with increasing voltage. This can be attributed to the trap state filling caused by charge injection.[27] The charge imbalance plays a negligible role on both PL and EL efficiencies here because of the low charging ratio. At voltages above 3 V, the PL intensity starts to drop in the two kinds of QD-LEDs, suggesting that the charging ratio is high enough to impact the PL efficiency. Nevertheless, the drop is much slower in the WZ-QD-LED, indicating that electron accumulation is less severe, and therefore Auger recombination and electron leakage are activated at higher voltages. This translates into the observed minimized efficiency roll-off of EQE in the WZ-QD-LED.
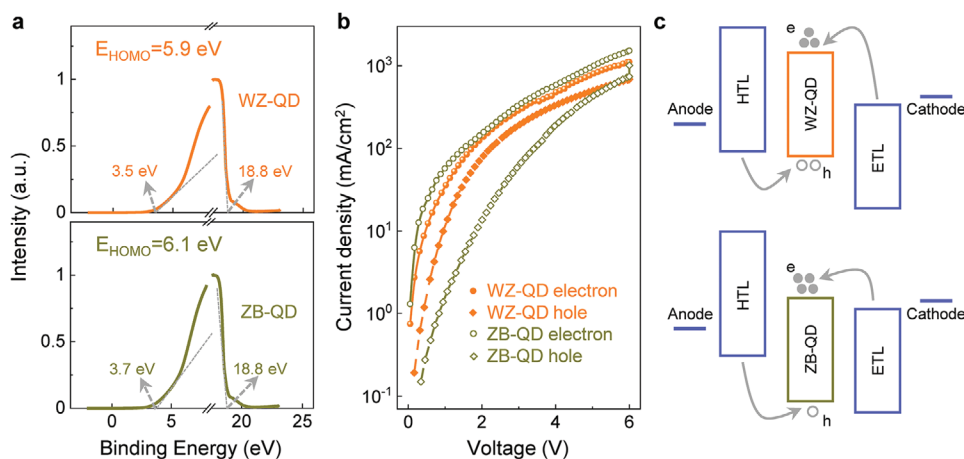
Figure 4. Electronic property characterizations of WZ- and ZB-QD. a), UPS spectra of WZ- (top panel) and ZB-QD (bottom panel). The HOMO energy level of ZB-QD is ≈0.2 eV higher than that of WZ-QD in the UPS spectra. b) Current density (J)-voltage (V) characteristics of electron-only and hole-only devices based on WZ- and ZB-QD. The electron current densities in both devices have similar results, while the hole current density in the WZ-QD device is obviously improved compared to the ZB-QD one, indicating a more balanced charge injection. c) Scheme of charge injection balance in the WZ- and ZB-QD devices.

Although the exact mechanism for the significantly improved operation stability of our QD-LED requires further research, the charge injection balance can certainly facilitate the device's performance. In addition, the operation voltage in WZ-QD-LED is quite low, suggesting high carrier injection efficiency and reduced Joule heating. Moreover, the operation voltage increases very slowly over time in the working WZ-QD-LED devices, indicating minimized charge accumulation and leakage (Figure S7, Supporting Information). All these factors can improve the device cyclability and prolong the operation lifetime in the WZ-QD-LED.

3. Conclusion

Our work unveils that the WZ- and ZB-QD behave remarkably different in their charge transport properties, regardless of their similarities in optical properties. The crystal-structure-dependent upshifted energy levels in the WZ-QD facilitate a more balanced charge injection. Thus, the observed crystal phase-engineered mechanism of QD in the working LED is expected to be applicable to QDs from other groups beyond II–V and III–V semiconductors, which will enable the elevation of comprehensive-performance LED to the level of commercialization.

4. Experimental Section

Stocks: Chemicals: Cadmium oxide (CdO, 99.99%), zinc acetate (Zn(AC)$_2$, 99.99%), selenium (Se, 99.99%, powder), sulfur (S, 99.998%, powder), oleic acid (OA, 90%), 1-octadecene (ODE, 90%), 1-octanethiol (OT, 98%), tri-n-octylphosphine (TOP; 97%), and dimethyl sulfoxide (DMSO, 99.7%) were purchased from Sigma Aldrich. Analytical-grade paraffin oil, methanol, and ethanol were obtained from Beijing Chemical Reagent Ltd., China. Acetone and N-hexane were obtained from Luoyang Chemical Reagent Ltd., China. Poly(9,9-dioctylfluorene-co-N-(4-(3-methylpropyl))diphenylamine) (TFB)) was purchased from American

Dye Source. Poly(3,4-ethylenedioxythiophene):polystyrene sulfonate (PEDOT:PSS) was purchased from Heraeus Deutschland GmbH & Co.KG.

Preparation of the WZ-Cd$_{1-x}$Zn$_x$Se /ZnSe$_y$S$_{1-y}$ QD: A mixture of 3.0 mmol Zn(AC)$_2$, 3.0 mmol CdO, 30 mL OA, and 10 mL paraffin oil was loaded into a three-neck flask. Next, the mixture was evacuated at 120 °C for 10 min and then heated to 330 °C under N$_2$ flow. Subsequently, the Se precursor (7.5 mmol in 4 mL TOP) was injected quickly to initiate the reaction. After the Cd$_{1-x}$Zn$_x$Se core reaction was completed in approximately 15 min, 10 mL Zn precursor was injected within 10 min followed by adding 10 mL Se-S precursor (rate of 0.2 mL min^{-1}). After the further reaction was completed within 20 min, the Cd$_{1-x}$Zn$_x$Se/ZnSe$_y$S$_{1-y}$ core/shell QDs were isolated by centrifugation using hexane, ethanol, and methanol. Finally, the QDs were dispersed in N-octane.

Preparation of the ZB-CdSe/Cd$_{1-x}$ZnxSe/ZnSe$_y$S$_{1-y}$ core/shell QDs: CdSe cores with a diameter of ≈3.5 nm were prepared using a modified version of a previously reported procedure. For the overcoating of Cd$_{1-x}$Zn$_x$Se, the desired amounts of Cd, Zn, and Se precursor were injected dropwise into the reaction solution with the temperature increasing to 330 °C. For further overcoating of the ZnSe shell, the desired amount of Zn and Se-S precursor (with equivalent amounts of Zn(OA)$_2$ and Se-S) was injected dropwise into the reaction solution. After finishing the precursor infusion, the solution was annealed at 300 °C for 30 min. Once the reaction was completed, the as-synthesized core/shell QDs were isolated by centrifugation using hexane, ethanol, and methanol. Then, the QDs were dispersed in N-octane.

Fabrication of the QD-LED: The glass substrate with a prepatterned indium tin oxide (ITO) anode was cleaned with deionized water, acetone, and isopropanol in an ultrasonication bath for 15 min in sequence. Subsequently, the ultrasonically cleaned ITO prepatterned substrate was treated in an ultraviolet ozone cleaner for 15 min. Then, the substrate was spin-coated with PEDOT:PSS (≈25 nm) at 5500 rpm for 30 s and baked at 140 °C for 30 min in air. After that, the PEDOT:PSS-coated substrate was immediately transferred to the nitrogen-filled glovebox. Approximately 20 nm TFB (6 mg mL^{-1} in chlorobenzene) was spin-coated at 3000 rpm and then annealed at 150 °C for 30 min. ≈35 nm QDs (18 mg mL^{-1} in octane) and 60 nm ZnO (50 mg mL^{-1} in ethanol) were spin-coated at 2000 rpm and then baked at 60 °C for 30 min. Finally, the aluminum cathode (100 nm) was thermally evaporated under a vacuum of <5 × 10^{-7} torr. The device was encapsulated by UV-curable resin in a glovebox.

Characterization and Instrumentation: UV–vis absorption and PL spectra were measured by an Ocean Optics spectrophotometer (model PC2000-ISA). All the QY data of the QD were collected through the

Ocean Optics USB2000 spectrometer and an Ocean Optics ISP-50-8-I integrating sphere. The optical density values of the QD samples at the excitation wavelength were all in the range of 0.02–0.05. The crystal structure of the QDs was studied by XRD 2θ scan on a D8-ADVANCE using Cu Kα radiation. The cross-section images of the QD-LED were obtained using an FEI Talos F200X TEM. HAADF-STEM images and EDS mappings were performed using an FEI Titan Themis G2 300 operating at 300 kV. UPS studies were performed on Thermo Scientific ESCALAB 250 XI equipment with a He I discharge lamp ($h\nu = 21.22$ eV). The current density-voltage (J–V) characteristics of the QD-LED were determined using an Agilent 4155C semiconductor parameter analyzer with a calibrated Newport silicon diode under ambient conditions. The luminance was calibrated using a Minolta luminance meter (LS-100) or Photo Research spectroradiometer (PR735 or PR650). The EL spectra were obtained with an Ocean Optics spectrometer (USB2000, relative irradiance mode) and a Keithley 2400 sourcemeter. In the operation time stability experiments, all the devices were encapsulated in commercially available ultraviolet-curing epoxy and cover glass and tested under ambient conditions (humidity of 30–40%, temperature of 21–25 °C). In situ PL and time-correlated single-photon counting (TCSPC) experiments were carried out with a customer-designed setup. The transient PL spectrum of QDs was excited using a Coherent Vitara-T oscillator and an optical parametric amplifier 9850 laser system (≈70 fs, 250 kHz, 400 nm). A Keithley 2400 sourcemeter and a 400 nm ultrafast pulsed laser were used for electrical and optical excitation, respectively. In addition, TCSPC and spectrograph systems were applied to record the transient PL lifetime and intensities, respectively.

Statistical Analysis: All data were presented in raw or standard format (mean ± standard deviation). Experimental data were collected by LabVIEW and Princeton SP2500 spectrometer software. All data were analyzed using MATLAB or Origin software. The Digital Micrograph software was used to process STEM and TEM images.

Supporting Information

Supporting Information is available from the Wiley Online Library or from the author.

Conflict of Interest

The authors declare no conflict of interest.

Data Availability Statement

The data that support the findings of this study are available from the corresponding author upon reasonable request.

[1] L. E. Brus, *J. Chem. Phys.* **1984**, *80*, 4403.
[2] V. L. Colvin, M. C. Schlamp, A. P. Alivisatos, *Nature* **1994**, *370*, 354.
[3] A. P. Alivisatos, *Science* **1996**, *271*, 933.
[4] S. Coe, W.-K. Woo, M. Bawendi, V. Bulović, *Nature* **2002**, *420*, 800.
[5] K.-S. Cho, E. K. Lee, W.-J. Joo, E. Jang, T.-H. Kim, *Nat. Photonics* **2009**, *3*, 341.
[6] X. Dai, Z. Zhang, Y. Jin, Y. Niu, H. Cao, *Nature* **2014**, *515*, 96.
[7] H. Shen, W. Cao, N. T. Shewmon, C. Yang, L. S. Li, *Nano Lett.* **2015**, *15*, 1211.
[8] W. Cao, C. Xiang, Y. Yang, Q. Chen, L. Chen, *Nat. Commun.* **2018**, *9*, 2608.
[9] Z. Shi, S. Li, Y. Li, H. Ji, X. Li, *ACS Nano* **2018**, *12*, 1462.
[10] H. Shen, Q. Gao, Y. Zhang, Y. Lin, Q. Lin, *Nat. Photonics* **2019**, *13*, 192.
[11] T. Kim, K.-H. Kim, S. Kim, S.-M. Choi, H. Jang, *Nature* **2020**, *586*, 385.
[12] M. Gao, H. Yang, H. Shen, Z. Zeng, F. Fan, *Nano Lett.* **2021**, *21*, 7252.
[13] F. P. García de Arquer, D. V. Talapin, V. I. Klimov, Y. Arakawa, M. Bayer, *Science* **2021**, *373*, eaaz8541.
[14] Y. Cheng, H. Wan, T. Liang, C. Liu, M. Wu, *J. Phys. Chem. Lett.* **2021**, *12*, 5967.
[15] H. Li, W. Zhang, Y. Bian, T. K. Ahn, H. Shen, *Nano Lett.* **2022**, *10*, 4067.
[16] T. Lee, B. J. Kim, H. Lee, D. Hahm, W. K. Bae, *Adv. Mater.* **2022**, *34*, 2106276.
[17] Y. Deng, F. Peng, Y. Lu, X. Zhu, W. Jin, *Nat. Photonics* **2022**, *16*, 505.
[18] J.-S. Kim, P. K. Ho, N. C. Greenham, R. H. Friend, *J. Appl. Phys.* **2000**, *88*, 1073.
[19] J. Lim, Y.-S. Park, K. Wu, H. J. Yun, V. I. Klimov, *Nano Lett.* **2018**, *18*, 6645.
[20] W. Nan, Y. Niu, H. Qin, F. Cui, Y. Yang, *J. Am. Chem. Soc.* **2012**, *134*, 19685.
[21] P. Klenovský, J. Valdhans, L. Krejčí, M. Valtr, P. Klapetek, *Electron. Struct* **2022**, *4*, 015006.
[22] M. Dong, J. Zhang, J. Yu, *APL Mater.* **2015**, *3*, 104404.
[23] H. Shen, H. Wang, Z. Tang, J. Z. Niu, S. Lou, *CrystEngComm* **2009**, *11*, 1733.
[24] J. Song, O. Wang, H. Shen, Q. Lin, Z. Li, *Adv. Funct. Mater.* **2019**, *29*, 1808377.
[25] S. Scholz, D. Kondakov, B. Lussem, K. Leo, *Chem. Rev.* **2015**, *115*, 8449.
[26] Y.-S. Park, W. K. Bae, L. A. Padilha, J. M. Pietryga, V. I. Klimov, *Nano Lett.* **2014**, *14*, 396.
[27] Y. Deng, X. Lin, W. Fang, D. Di, L. Wang, *Nat. Commun.* **2020**, *11*, 2309.

[28] P. Steindl, E. M. Sala, B. Alén, D. Bimberg, P. Klenovský, *New J. Phys.* **2021**, *23*, 103029.

[29] Y. Shirasaki, G. J. Supran, W. A. Tisdale, V. Bulović, *Phys. Rev. Lett.* **2013**, *110*, 217403.

[30] W. Zou, R. Li, S. Zhang, Y. Liu, N. Wang, Y. Cao, Y. Miao, M. Xu, Q. Guo, D. Di, L. Zhang, C. Yi, F. Gao, R. H. Friend, J. Wang, W. Huang, *Nat. Commun.* **2018**, *9*, 608.

[31] H. Huang, D. Csontosová, S. Manna, Y. Huo, R. Trotta, *Phys. Rev. B* **2021**, *104*, 165401.

[32] B. G. Jeong, J. H. Chang, D. Hahm, S. Rhee, M. Park, S. Lee, Y. Kim, D. Shin, J. W. Park, C. Lee, D. C. Lee, K. Park, E. Hwang, W. K. Bae, *Nat. Mater.* **2022**, *21*, 246.

[33] B. S. Mashford, M. Stevenson, Z. Popovic, C. Hamilton, Z. Zhou, *Nat. Photonics* **2013**, *7*, 407.